



Article

Enhancement of Casimir Friction between Graphene-Covered Topological Insulator

Ting Yu, Rong Luo, Tongbiao Wang *, Dejian Zhang, Wenxing Liu, Tianbao Yu and Qinghua Liao

Department of Physics, Nanchang University, Nanchang 330031, China; Yutingncu157@163.com (T.Y.); luorong_jjvc@163.com (R.L.); zhangdejian2015@163.com (D.Z.); liuwenxing@ncu.edu.cn (W.L.); yutianbao@ncu.edu.cn (T.Y.); lqhua@ncu.edu.cn (Q.L.)

* Correspondence: tbwang@ncu.edu.cn

Abstract: Casimir friction is theoretically studied between graphene-covered undoped bismuth selenide (Bi_2Se_3) in detail. In the graphene/ Bi_2Se_3 composite structure, the coupling of the hyperbolic phonon polaritons supported by Bi_2Se_3 with the surface plasmons supported by graphene can lead to the hybrid surface plasmon–phonon polaritons (SPPPs). Compared with that between undoped Bi_2Se_3 , Casimir friction can be enhanced by more than one order of magnitude due to the contribution of SPPPs. It is found that the chemical potential that can be used to modulate the optical characteristic of SPPPs plays an important role in Casimir friction. In addition, the Casimir friction between doped Bi_2Se_3 is also studied. The friction coefficient between doped Bi_2Se_3 can even be larger than that between graphene-covered undoped Bi_2Se_3 for suitable chemical potential due to the contribution of unusual electron surface states. The results obtained in this work are not only beneficial to the study of Casimir frictions but also extend the research ranges of topological insulators.

Keywords: casimir friction; graphene; topological insulator



Citation: Yu, T.; Luo, R.; Wang, T.; Zhang, D.; Liu, W.; Yu, T.; Liao, Q. Enhancement of Casimir Friction between Graphene-Covered Topological Insulator. *Nanomaterials* **2022**, *12*, 1148. <https://doi.org/10.3390/nano12071148>

Academic Editors: Xiewen Wen, Elena D. Obratsova, Filippo Giubileo and Gongxun Bai

Received: 17 January 2022

Accepted: 28 March 2022

Published: 30 March 2022

Publisher's Note: MDPI stays neutral with regard to jurisdictional claims in published maps and institutional affiliations.



Copyright: © 2022 by the authors. Licensee MDPI, Basel, Switzerland. This article is an open access article distributed under the terms and conditions of the Creative Commons Attribution (CC BY) license (<https://creativecommons.org/licenses/by/4.0/>).

1. Introduction

In nature, friction is a very common phenomenon, which extensively exists in the macroscopic to the microscopic world. However, the physical mechanism of friction in the microscopic world is different from that of the friction observed in our daily lives. In recent years, people have paid much attention to nanotribology with the rapid development of nanofabrication technology. Interestingly, there is one type of friction that appears between bodies in relative motion even without direct contact at the nanoscale, which is usually called noncontact friction [1–7]. Noncontact friction has been observed experimentally by atomic force microscopy [1,5,6] and has important practical significance in ultra-sensitive force detection. In the past decade, another noncontact friction originating from the momentum exchange of Doppler-shifted photons has attracted much attention [8]. The essence of this friction is closely related to the Casimir effect, so it is called Casimir friction [8,9]. Even at zero temperature, Casimir friction can still exist because of the vacuum fluctuation, so it will be denoted as quantum friction. Casimir frictions have been extensively studied in several configurations that are in relative motion, such as atom and atom [10], atom and plate [11–13], and plate and plate [14].

The theoretical method of Casimir friction between two objects separated by a small gap was firstly derived by Pendry with the help of classical electromagnetic theory [8]. Then, Volokitin and Persson also made a series of works on Casimir friction [15–20]. Because the Casimir friction is extremely small, it makes a great challenge to detect in an experiment. Enhancing the Casimir friction between bodies in relative motion becomes an important topic. An enhancement mechanism of Casimir friction associated with resonant photon tunneling on different surfaces was proposed [16]. It has been found that Casimir friction will be significantly enhanced if the materials can support low-frequency surface plasmons (SPs) or other surface polaritons [16]. Therefore, plenty of materials that can support

surface polaritons are employed to investigate the Casimir friction [21,22]. Among them, graphene is a two-dimensional material composed of carbon atoms [23–25], which can support SPs from terahertz (THz) to infrared frequency ranges [26–35]. In particular, the optical conductivity of graphene depends on its chemical potential, which is controlled by an external field or gate voltage. It is shown that SPs supported by graphene can play an important role in enhancing and actively modulating Casimir friction [36–39]. In addition, the Casimir friction between graphene-covered hyperbolic materials (HMs) has also been studied [40]. The coupling of graphene plasmon with hyperbolic phonon polaritons (HPPs) supported by HMs can enhance the Casimir friction remarkably [40].

In the past decade, topological insulators have received extensive attention because of their exotic characteristic and important applications in the fabrications of new electronic devices [41–45]. They are characterized by a full insulating gap in the bulk and gapless surface states protected by time-reversal symmetry [44]. The three-dimensional (3D) topological insulators have been predicted theoretically in the $\text{Bi}_{1-x}\text{Sb}_x$ alloy [46] and observed experimentally by angle-resolved photoemission spectroscopy [47]. Then, several simple 3D topological insulators were predicted theoretically in Bi_2Te_3 , Sb_2Te_3 [48], and Bi_2Se_3 [48,49] compounds with a large gap in bulk and gapless surface state. Bismuth-based topological insulators have attracted great interest due to their unusual electronic surface states, which are manifested as massless Dirac fermions [43,44,48–51]. As one of the representative topological insulators, Bi_2Se_3 is also well-known for its bulk optical response [52–55] besides its novel surface state. It exhibits hyperbolic dispersion relation and can support highly oriented collective HPPs in the THz range [56]. For Bi_2Se_3 with finite doping, the coupling of HPPs with Dirac plasmon confined at the surface can result in the appearance of hybrid modes [56]. However, the SPs are absent for undoped Bi_2Se_3 . As has been mentioned above, graphene plasmon can be coupled with different surface polaritons, so it is interesting to investigate the coupling between graphene plasmon and HPPs supported by undoped Bi_2Se_3 .

In this paper, we study the Casimir friction between graphene-covered undoped Bi_2Se_3 . The low-frequency HPPs supported by Bi_2Se_3 can be coupled with SPs supported by graphene, and then resulting in the appearance of hybrid surface plasmon–phonon polaritons (SPPPs). We demonstrate that the SPPPs play an important role in the Casimir friction between graphene-covered Bi_2Se_3 . Compared with that between undoped Bi_2Se_3 , the Casimir friction between graphene-covered Bi_2Se_3 enhances about one order of magnitude in wide separation gaps. Furthermore, the hybrid SPPPs can be flexibly controlled by tuning the chemical potential of graphene that depends on the gate voltage. Therefore, it provides an opportunity to actively modulate the Casimir friction between topological insulators. Casimir friction between doped Bi_2Se_3 is also studied. Depending on the chemical potential, Casimir friction between doped Bi_2Se_3 can be larger or smaller than that between graphene-covered Bi_2Se_3 under the same separation distance. This study not only extends the research ranges of topological insulators but also provides an efficient method to control the Casimir friction.

2. Theoretical Model

The schematic of the Casimir force between graphene-covered Bi_2Se_3 is shown in Figure 1. Two graphene-covered Bi_2Se_3 bulks are separated by a distance d . We assume the top graphene-covered Bi_2Se_3 moves relatively to the bottom one along the x -axis with a velocity v in the laboratory frame. The temperature of the surrounding environment is denoted by T , which is set to be $T = 300$ K in all the calculations. If the moving velocity of the top graphene-covered Bi_2Se_3 satisfies the conditions $v < dk_B T / \hbar$, Casimir friction is proportional to the sliding velocity, which can be determined as $f = \gamma v$ [18]. k_B and \hbar are the Boltzmann and reduced Planck constants, respectively. $\gamma = \gamma^{\text{rad}} + \gamma^{\text{evan}}$ is the Casimir friction coefficient, which comes from the contributions of propagation and evanescent electromagnetic waves from the graphene-covered Bi_2Se_3 . However, the contribution of the propagation wave can be ignored in the near-field region [2,18]. Therefore, we only

consider the Casimir friction coefficient from the evanescent waves, which can be expressed as [18]

$$\gamma \approx \frac{\hbar}{2\pi^2} \int_0^\infty d\omega \left(-\frac{\partial n}{\partial \omega} \right) \int_{\omega/c}^\infty dq q^3 e^{-2|k_z|d} \frac{\text{Im}(R_{1p})\text{Im}(R_{2p})}{|1 - e^{-2|k_z|d} R_{1p} R_{2p}|^2} + [p \rightarrow s] \quad (1)$$

where $n(\omega) = 1/(e^{\hbar\omega/k_B T} - 1)$ is the Bose–Einstein factor. q and $k_z = \sqrt{(\omega/c)^2 - q^2}$ are the components of the wave vector components parallel and perpendicular to the xy plane, respectively. c is the speed of light in the vacuum and R_{ip} ($i = 1,2$) is the reflection amplitude from the top or bottom surface of the p -polarized electromagnetic waves. The symbol $[p \rightarrow s]$ represents the p -polarized reflection amplitude R_p replaced with s -polarized reflection amplitude R_s . As described in Ref. [57], p -polarized wave often plays a dominant role in the near-field region, so the contribution from s -polarized waves can be excluded. The integral of q in Equation (1) is defined as force spectral density (FSD), which can be expressed by

$$f_p = -\frac{\partial n}{\partial \omega} \int_{\omega/c}^\infty dq q^3 \frac{\text{Im}(R_{1p})\text{Im}(R_{2p})}{|1 - e^{-2|k_z|d} R_{1p} R_{2p}|^2} e^{-2|k_z|d} \quad (2)$$

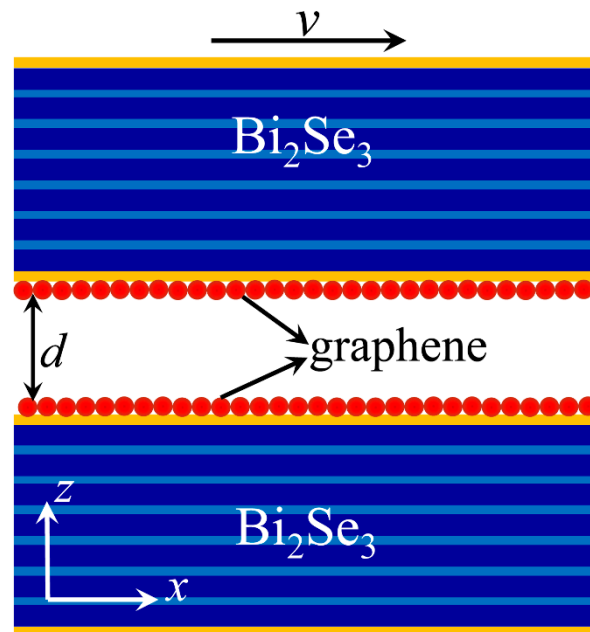


Figure 1. Schematic of Casimir friction between graphene-covered undoped Bi_2Se_3 separated by a distance d . The layered structure denotes Bi_2Se_3 and the two thin orange layers at the top and bottom of Bi_2Se_3 represent the surface states.

For convenient description, we define the photon exchange function as

$$\tilde{\zeta}_p = \frac{\text{Im}(R_{1p})\text{Im}(R_{2p})}{|1 - e^{-2|k_z|d} R_{1p} R_{2p}|^2} e^{-2|k_z|d} \quad (3)$$

which is used to describe the exchange ability of photons between the bodies in relative motion. The reflection amplitude of graphene-covered anisotropic material can be written as [58]

$$R_p = \frac{p\epsilon^\perp - p_p + \mu_0 c \sigma p p_p}{p\epsilon^\perp + p_p + \mu_0 c \sigma p p_p} \quad (4)$$

where $p = \sqrt{1 - \kappa^2}$, $p_p = \sqrt{\epsilon^\perp - \epsilon^\perp \kappa^2 / \epsilon^z}$, and $\kappa = cq/\omega$. ϵ^z and ϵ^\perp are the permittivities of Bi_2Se_3 parallel and perpendicular to the optical axis (z -axis), respectively. μ_0 is the permeability in the vacuum. $\sigma(\omega)$ is the optical conductivity of graphene, which can be simplified to $\sigma = \frac{ie^2\mu}{\pi\hbar^2(\omega+i\tau^{-1})}$ in the low-frequency range by ignoring the contribution of interband transitions [32]. e is the electron charge, μ is the chemical potential of graphene, and $\tau = 10^{-13}$ s is the relaxation time. As a naturally anisotropic material, Bi_2Se_3 exhibits hyperbolic optical properties. The dielectric properties perpendicular (ϵ^\perp) and parallel (ϵ^z) to the optical axis have different values which are given by [59,60]

$$\epsilon^\alpha(\omega) = \epsilon_\infty^\alpha + \sum_{j=1,2} \frac{\omega_{p,j}^{\alpha 2}}{\omega_{to,j}^{\alpha 2} - \omega^2 - i\gamma_j^\alpha \omega}, (\alpha = \perp, z) \tag{5}$$

The parameters used in Equation (5) are $\epsilon_\infty^\perp = 29$, $\epsilon_\infty^z = 17.4$, $\omega_{to,1}^\perp = 64 \text{ cm}^{-1}$, $\omega_{p,1}^\perp = 704 \text{ cm}^{-1}$, $\omega_{to,2}^\perp = 125 \text{ cm}^{-1}$, $\omega_{p,2}^\perp = 55 \text{ cm}^{-1}$, $\omega_{to,1}^z = 135 \text{ cm}^{-1}$, $\omega_{p,1}^z = 283 \text{ cm}^{-1}$, $\omega_{to,2}^z = 154 \text{ cm}^{-1}$, $\omega_{p,2}^z = 156 \text{ cm}^{-1}$, $\gamma_j^\alpha = 3.5 \text{ cm}^{-1}$. The real parts of the dielectric functions $\epsilon^\perp(\omega)$ and $\epsilon^z(\omega)$ of Bi_2Se_3 are shown in Figure 2. There are two shaded regions, including regions A ($\omega_{to,1}^\perp < \omega < \omega_{to,1}^z$) where Bi_2Se_3 is type II HM ($\text{Re}(\epsilon^z) > 0, \text{Re}(\epsilon^\perp) < 0$) and region B ($\omega_{to,2}^z < \omega < 163 \text{ cm}^{-1}$) where Bi_2Se_3 is type I HM ($\text{Re}(\epsilon^z) < 0, \text{Re}(\epsilon^\perp) > 0$). Therefore, HPPs can be excited in these hyperbolic regions [56]. Although as a typical topological insulator, Bi_2Se_3 possesses unusual electron surface states, we firstly only consider its bulk optical response. When the frequencies are smaller than the bulk gap of 0.3 eV of Bi_2Se_3 , the electronic contribution to permittivities (appearing in Equation (5) via ϵ_∞^α) is purely real. In addition, it is assumed that the valence bulk band is completely filled and the conduction band is empty, there are no free carriers present in the bulk. The doping electron surface states of Bi_2Se_3 is determined by its chemical potential μ_B that is located inside the bulk band gap. The electron surface states can be excluded by setting $\mu_B = 0.0$ eV.

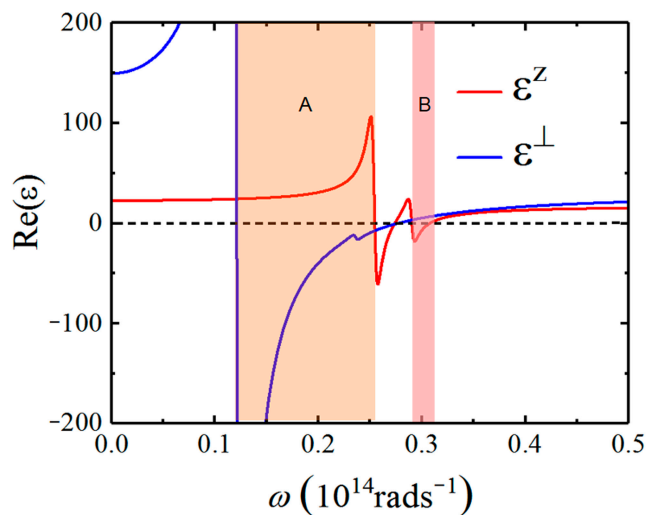


Figure 2. The real part of the dielectric function of Bi_2Se_3 . The shaded regions denote the hyperbolic regions. Regions A and B denote type II ($\text{Re}(\epsilon^\perp) < 0, \text{Re}(\epsilon^z) > 0$) and type I ($\text{Re}(\epsilon^\perp) > 0, \text{Re}(\epsilon^z) < 0$) hyperbolic bands, respectively.

3. Casimir Friction between Graphene-Covered Bi_2Se_3

In Figure 3, we show the dependences of Casimir friction on distance d for different configurations. As a natural hyperbolic material, hBN can also support HPPs which are located in the infrared regions. The permittivities of hBN can be found in Ref. [58]. Here we also show the Casimir friction between hBN bulk for comparison. The results

of hBN, Bi₂Se₃, graphene, and graphene-covered Bi₂Se₃ are denoted in green dotted, red dashed, blue dot-dashed, and black solid lines, respectively. The chemical potential of graphene is fixed at $\mu = 0.2$ eV. It is seen that the Casimir friction coefficients of different configurations decrease as the distance increases. The friction coefficients of graphene and Bi₂Se₃ decrease slowly as the distance increases, while the friction coefficients of hBN and graphene-covered Bi₂Se₃ decrease rapidly as the distance increases. Although the friction coefficient of Bi₂Se₃ is smaller than that of hBN when the distance is less than 25 nm, it has an obvious enhancement when covered with graphene. Compared with that of Bi₂Se₃, the friction coefficient between graphene-covered Bi₂Se₃ can increase more than one order of magnitude when the chemical potential of graphene is 0.2 eV.

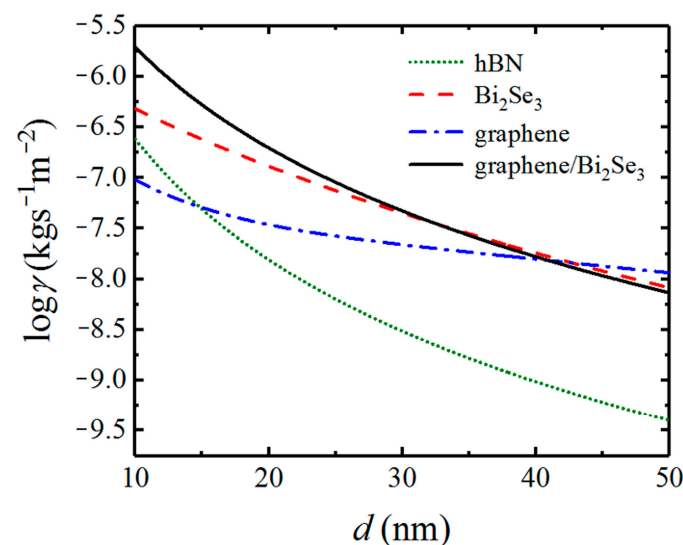


Figure 3. The dependence of Casimir friction coefficients for different configurations on separation distance d . The chemical potential of graphene is $\mu = 0.2$ eV. The base of the logarithm is 10 in this and the following figures.

Because Casimir friction is mainly from the exchange of the evanescent waves in the near-field region, we display the FSDs for different configurations to realize the contribution of different evanescent waves to Casimir friction in Figure 4. The results of hBN, Bi₂Se₃, graphene, and graphene-covered Bi₂Se₃ are displayed in green dotted, red dashed, blue dot-dashed, and black solid lines, respectively. The chemical potential of graphene is set to be $\mu = 0.2$ eV and the separation distance is $d = 20$ nm. It can be clearly seen from Figure 4 that there are two peaks corresponding to its hyperbolic bands located in the infrared frequency region for the FSD of hBN. Similarly, there are two peaks in the low-frequency regions for Bi₂Se₃. FSD has a strong peak corresponding to the resonance frequency of the HPPs on the surface of Bi₂Se₃ material, so the main contribution to quantum friction in Bi₂Se₃ comes from the HPPs. The FSD spectrum of graphene covers a very wide frequency range but with a relatively low value, which agrees that graphene can support p -polarized SPs with a wide frequency range. For graphene-covered undoped Bi₂Se₃, the HPPs supported by Bi₂Se₃ can be coupled with SPs supported by graphene, which results in the shift of the hybrid SPPs toward higher frequencies. Therefore, the Casimir friction between graphene-covered Bi₂Se₃ is mainly from the SPPs. We can qualitatively obtain the Casimir friction by judging the area covered by the curves of different configurations.

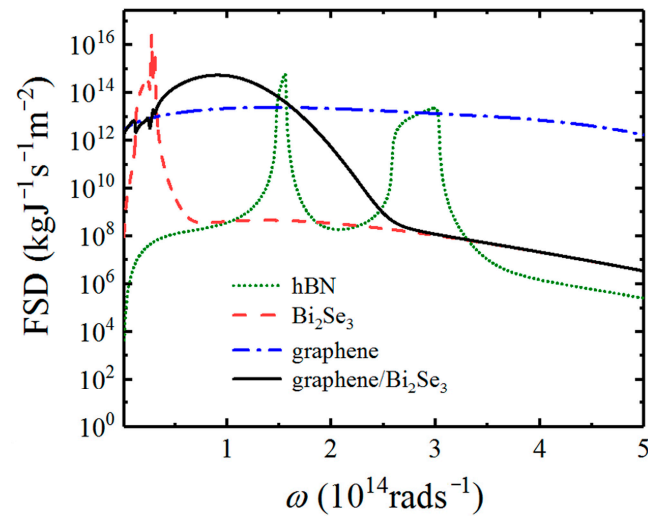


Figure 4. The force spectral densities for different configurations. The parameters used here are the same as those used in Figure 3.

To further analyze the physical mechanism of Casimir frictions for different configurations, we show the photon exchange functions of these configurations in Figure 5. The bright regions in the dark background denote the different surface polaritons supported by different materials. In Figure 5a, the bright regions are from the contributions of type I and type II hyperbolic bands of hBN, respectively. For the case of Bi_2Se_3 shown in Figure 5b, we can see that the hyperbolic bands also exist in the THz frequency range. For the photon exchange function between graphene sheets shown in Figure 5c, it covers a very wide frequency range since graphene can support SPs from THz to infrared frequencies. When Bi_2Se_3 is covered with graphene, the HPPs supported by Bi_2Se_3 can couple with SPs supported by graphene to form the SPPPs which is out of the hyperbolic band. The SPPPs move toward higher frequencies as the wave vector increases. Therefore, we can obtain that SPPPs dominate the Casimir friction between graphene-covered undoped Bi_2Se_3 .

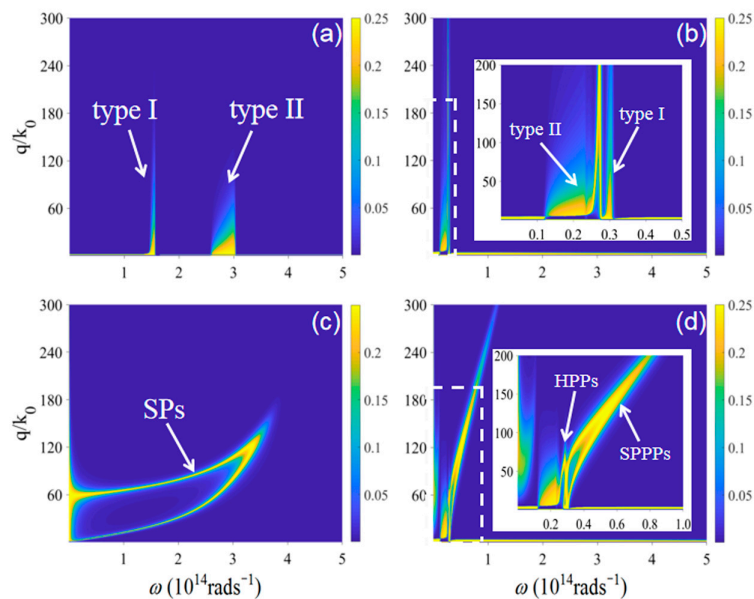


Figure 5. The photon exchange functions in different configurations. (a): hBN; (b): Bi_2Se_3 ; (c): graphene; (d): graphene-covered Bi_2Se_3 . The chemical potential of graphene is $\mu = 0.2$ eV and the separation distance is $d = 20$ nm. The insets in (b,d) are the enlarged areas denoted by white dashed lines.

Because the characteristic of SPs excited by graphene as well as the coupled SPPs is dependent on the chemical potential of graphene, we investigate the effect of chemical potential on the Casimir friction. In Figure 6, we display the friction coefficient on the separation distance d for different chemical potentials of graphene. The friction coefficient between graphene-covered Bi_2Se_3 with chemical potentials $\mu = 0.1$, $\mu = 0.2$, and $\mu = 0.3$ eV are plotted in black solid, blue dashed, and red dotted lines, respectively. We can see that the friction coefficients varying with distance exhibit different behavior for different chemical potentials. As the distance increases, the difference of Casimir friction between systems with different chemical potentials becomes smaller, which means that the contribution from the evanescent SPPs becomes weaker as the distance increases.

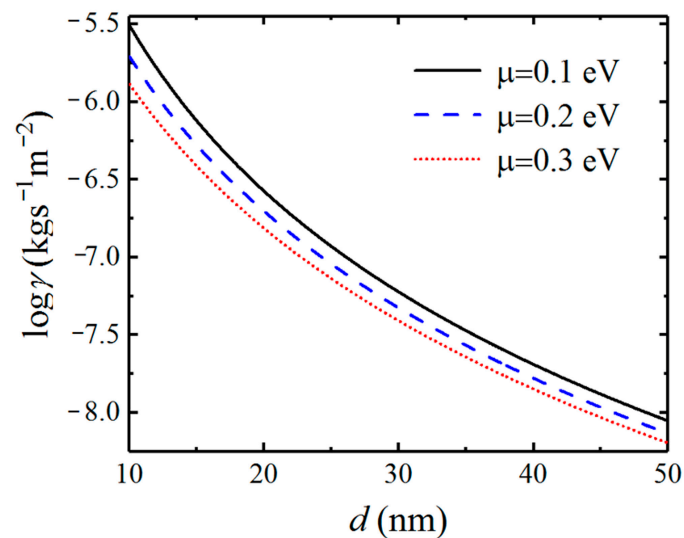


Figure 6. Dependence of the Casimir friction coefficient between graphene-covered Bi_2Se_3 on the separation distance for different chemical potentials of graphene.

In Figure 7, we show the dependence of the friction coefficient on the chemical potential between graphene-covered Bi_2Se_3 bulks. The friction coefficients with separation distances of 10, 20, and 30 nm are plotted in black solid, blue dashed, and red dotted lines, respectively. In Figure 7, we can see that the friction coefficients increase first and then decrease after reaching the maximum values as the chemical potential increases. In particular, the difference between the maximum value and minimum value of friction coefficients can reach about one order of magnitude for different chemical potentials for the separation distance being 10 nm. When the separation distance increases, the maximum and minimum values of Casimir friction still have an obvious difference in our considered chemical potential range. Therefore, the maximum value of the friction coefficient can be obtained by tuning the chemical potential of graphene.

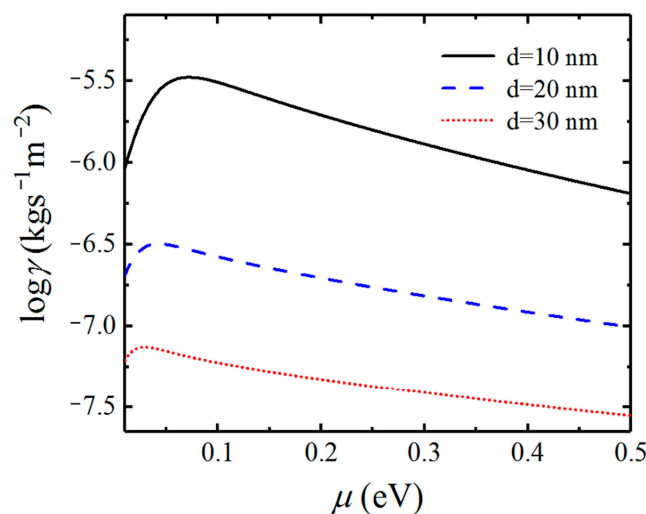


Figure 7. Dependence of the Casimir friction coefficient on chemical potential for different separation distances d .

In Figure 8, we show the FSD in order to understand the physical mechanism of the relationship between the friction coefficient and chemical potential. The separation distance between the top and bottom graphene-covered Bi_2Se_3 is fixed at $d = 20$ nm in the calculations. When the chemical potential of graphene is smaller ($\mu = 0.05$ eV), we can see that Casimir friction is mainly determined by the HPPs as shown by the solid black line. In this case, the coupling between HPPs and graphene plasmons is weak. The HPPs and graphene plasmon contribute to the Casimir friction separately. As the chemical potential increases ($\mu = 0.1$ eV), the coupling between HPPs and SPs occurs, resulting in the enhancement of SPPs in a wide frequency region compared with the SPs supported by graphene as shown in red dashed lines in Figure 8. However, when the chemical potential continues to increase, the peak of SPPs shifts toward higher frequencies with a decrease in magnitude. This will lead to the decrease in the Casimir friction. Therefore, we can demonstrate the coupling of graphene plasmon with HPPs supported by undoped Bi_2Se_3 can enhance the Casimir friction significantly between graphene-covered Bi_2Se_3 . It is also possible to actively modulate the Casimir friction between such graphene/ Bi_2Se_3 composite structures by controlling the gate voltage.

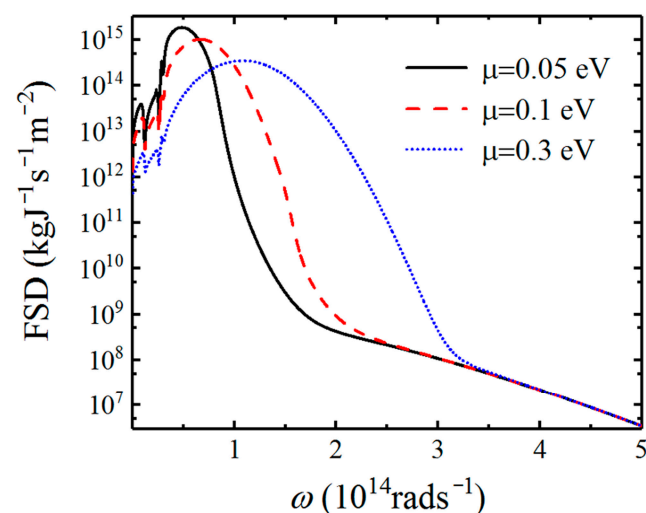


Figure 8. Force spectral densities of graphene-covered Bi_2Se_3 as a function of angular frequency for different chemical potentials at a fixed distance $d = 20$ nm.

4. Casimir Friction between Doped Bi₂Se₃ Bulks

We have investigated the Casimir friction between graphene-covered undoped Bi₂Se₃ in the previous sections. Then, we continue to study the Casimir friction between doped Bi₂Se₃ without covering graphene. Such a configuration can be realized by moving graphene away in Figure 1. In this configuration, the Bi₂Se₃ bulk behaves like an anisotropic material, while the two layers denoted in orange represent the top and bottom surface states. The electron surface states which behave as massless Dirac fermions exist when Bi₂Se₃ is doped; it plays a similar role as graphene in the graphene-covered undoped Bi₂Se₃ configuration. The fundamental density response functions of the surface states are the sheet conductivity σ_B and polarizability P , which have the following relation [56]

$$\sigma_B(q, \omega) = \frac{i\omega}{q^2} e^2 P(q, \omega) \quad (6)$$

Under the condition of random-phase approximation for Dirac fermions, $P(q, \omega)$ can be obtained analytically [56]:

$$P(q, \omega) = -\frac{Nk_F}{2\pi\hbar v_F} - \frac{iN}{16\pi\hbar v_F} \frac{q^2}{\sqrt{q^2 - k_\omega^2}} \left[G\left(\frac{k_\omega + 2k_F}{q}\right) - G\left(\frac{k_\omega - 2k_F}{q}\right) - i\pi \right] \quad (7)$$

where function $G(x)$ are expressed as $G(x) = ix\sqrt{1 - x^2} - i\arccos x$. $N = 1$ is the number of Dirac cones. $k_F = |\mu_B|/\hbar v_F$ is the Fermi momentum with $v_F = \sqrt{\mu_{dc}\mu_B\tau_B}/e$ being the Fermi velocity, and μ_{dc} is the electron mobility. $k_\omega = (\omega + i\gamma_e)/v_F$ and $\gamma_e > 0$ is a phenomenological parameter that stands for electron scattering rate. After substituting the conductivity in Equation (4) with σ_B in Equation (6), we can calculate the Casimir friction between doped Bi₂Se₃ by employing Equation (1).

In Figure 9, we show the dependence of the Casimir friction coefficient on the separation distance d for different chemical potentials μ_B of doped Bi₂Se₃, which is similar to that shown in Figure 6. We can see that the Casimir friction coefficient decreases rapidly with the increase in separation distance d . When the separation distance is less than 20 nm, the friction coefficient is not sensitive to the chemical potential. When the separation distance becomes larger, the friction coefficient decreases as the chemical potential increases. Such phenomenon is different from that between graphene-covered undoped Bi₂Se₃ which is shown in Figure 6. In addition, comparing Figure 9 with Figure 3, we can also see that the friction coefficient between doped Bi₂Se₃ is larger than that between undoped Bi₂Se₃ when the separation distance is less than 20 nm. However, when the separation is larger than 20 nm, the difference in Casimir friction between undoped Bi₂Se₃ and doped Bi₂Se₃ is very small.

In Figure 10, we show the dependence of the Casimir friction coefficient on the chemical potential of doped Bi₂Se₃ for different separation distances d . When the separation distance is 10 nm, the friction coefficient almost does not vary with the chemical potential. That means the chemical potential of doped Bi₂Se₃ has little impact on the surface states that dominate the Casimir friction at such a small distance. The Casimir friction, in this case, is even larger than that between graphene-covered Bi₂Se₃ when the chemical potential is larger than 0.1 eV, which can be seen in Figure 7. For the cases with separation distances are 20 and 30 nm, the friction coefficients first increase and then decrease after reaching the maximum values as the chemical potential μ_B increase. However, the friction coefficients between doped Bi₂Se₃ are not as sensitive to the chemical potential as those between graphene-covered undoped Bi₂Se₃.

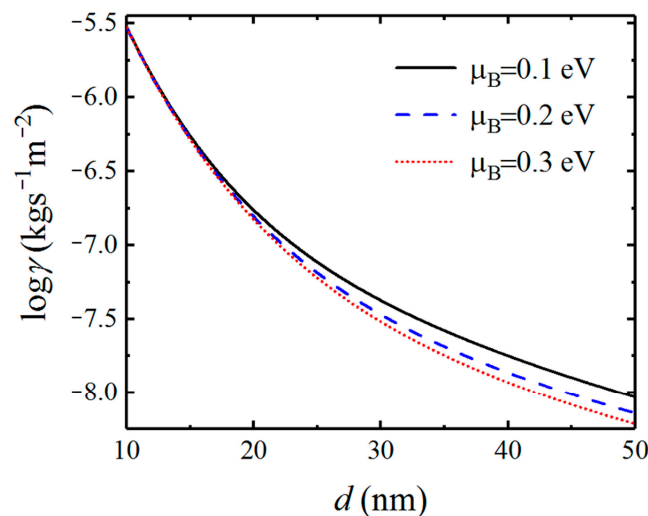


Figure 9. Dependence of the Casimir friction coefficient on the separation distances for different chemical potentials of Bi_2Se_3 .

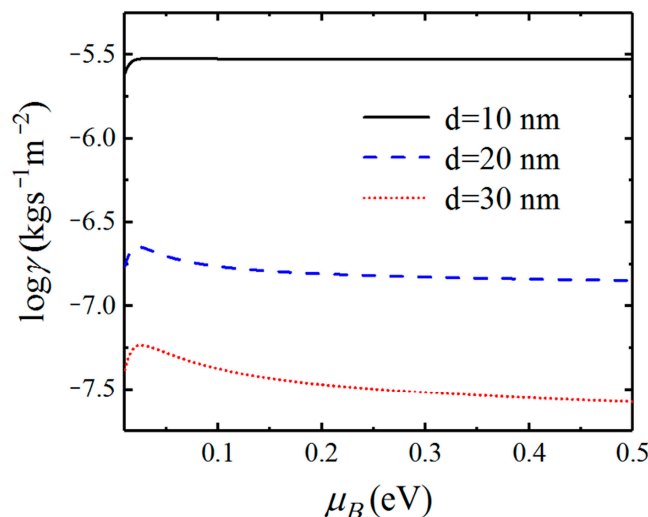


Figure 10. Dependence of the Casimir friction coefficient on chemical potential for different separation distances d .

5. Conclusions

In summary, we have studied the Casimir friction between graphene-covered Bi_2Se_3 . Owing to the coupling of the HPPs supported by Bi_2Se_3 to the SPs excited by graphene, the Casimir friction between the proposed structures shows a significant enhancement compared to those between undoped Bi_2Se_3 materials. The Casimir friction can be modulated actively by tuning the chemical potential of graphene. It is found that the maximum value of Casimir friction can be obtained by choosing the appropriate chemical potential. Furthermore, Casimir friction between doped Bi_2Se_3 is also studied. When the chemical potential is larger than 0.1 eV, Casimir friction between doped Bi_2Se_3 is even larger than that between graphene-covered undoped Bi_2Se_3 . Although more and more schemes have been proposed to enhance the Casimir force, it is still challenging to observe such a small force exactly in an experiment. Because it may play an important role in the nanoelectromechanical systems (NEMS), it is feasible to observe the Casimir force in the NEMS successfully. The results of this study are of great help to extend the research range of Casimir frictions and are meaningful to understanding the application of ultra-sensitive force detection of topological insulators.

Author Contributions: The manuscript was written through contributions of all authors. Conceptualization, T.Y. (Ting Yu) and R.L.; methodology, T.W. and T.Y. (Tianbao Yu); data curation, T.Y. (Ting Yu); validation, D.Z. and W.L.; writing—original draft preparation, T.Y. (Ting Yu); writing—review and editing, T.W.; supervision, Q.L.; funding acquisition, T.W. All authors have read and agreed to the published version of the manuscript.

Funding: This work is supported by the National Natural Science Foundation of China (Grant Nos. 12164027, 11704175, 12064025).

Institutional Review Board Statement: Not applicable.

Informed Consent Statement: Not applicable.

Data Availability Statement: The data that support the findings of this study are available upon reasonable request from the corresponding author.

Conflicts of Interest: The authors declare no conflict of interest.

References

1. Dorofeyev, I.; Fuchs, H.; Wenning, G.; Gotsmann, B. Brownian Motion of Microscopic Solids under the Action of Fluctuating Electromagnetic Fields. *Phys. Rev. Lett.* **1999**, *83*, 2402. [[CrossRef](#)]
2. Volokitin, A.I.; Persson, B.N.J. Noncontact friction between nanostructures. *Phys. Rev. B* **2003**, *68*, 155420. [[CrossRef](#)]
3. She, J.H.; Balatsky, A.V. Non-contact Friction and Relaxational Dynamics of Surface Defects. *Phys. Rev. Lett.* **2012**, *108*, 136101. [[CrossRef](#)]
4. Jentschura, U.D.; Janke, M.; DeKieviet, M. Theory of noncontact friction for atom-surface interactions. *Phys. Rev. A* **2016**, *94*, 022510. [[CrossRef](#)]
5. Stipe, B.C.; Mamin, H.J.; Stowe, T.D.; Kenny, T.W.; Rugar, D. Noncontact Friction and Force Fluctuations between Closely Spaced Bodies. *Phys. Rev. Lett.* **2001**, *87*, 096801. [[CrossRef](#)] [[PubMed](#)]
6. Kuehn, S.; Loring, R.F.; Marohn, J.A. Dielectric Fluctuations and the Origins of Noncontact Friction. *Phys. Rev. Lett.* **2006**, *96*, 156103. [[CrossRef](#)]
7. Saitoh, K.; Hayashi, K.; Shibayama, Y.; Shirahama, K. Gigantic Maximum of Nanoscale Noncontact Friction. *Phys. Rev. Lett.* **2010**, *105*, 236103. [[CrossRef](#)]
8. Pendry, J. Shearing the vacuum—quantum friction. *J. Phys. Condens. Matter* **1997**, *9*, 10301–10320. [[CrossRef](#)]
9. Fariás, M.B.; Fosco, C.D.; Lombardo, F.; Mazzitelli, F.; López, A.E.R. Functional approach to quantum friction: Effective action and dissipative force. *Phys. Rev. D* **2015**, *91*, 105020. [[CrossRef](#)]
10. Barton, G. On van der Waals friction between two atoms at nonzero temperature. *New J. Phys.* **2011**, *13*, 043023. [[CrossRef](#)]
11. Reiche, D.; Dalvit, D.A.R.; Busch, K.; Intravaia, F. Spatial dispersion in atom-surface quantum friction. *Phys. Rev. B* **2017**, *95*, 155448. [[CrossRef](#)]
12. Zhao, R.; Manjavacas, A.; de Abajo, F.J.G.; Pendry, J. Rotational Quantum Friction. *Phys. Rev. Lett.* **2012**, *109*, 123604. [[CrossRef](#)] [[PubMed](#)]
13. Manjavacas, A.; Rodríguez-Fortuño, F.J.; de Abajo, F.J.G.; Zayats, A.V. Lateral Casimir Force on a Rotating Particle near a Planar Surface. *Phys. Rev. Lett.* **2017**, *118*, 133605. [[CrossRef](#)]
14. Høyevik, J.S.; Brevik, I. Casimir friction between a magnetic and a dielectric material in the nonretarded limit. *Phys. Rev. A* **2019**, *99*, 042511. [[CrossRef](#)]
15. Volokitin, A.I.; Persson, B.N.J. Dissipative van der Waals interaction between a small particle and a metal surface. *Phys. Rev. B* **2002**, *65*, 115419. [[CrossRef](#)]
16. Volokitin, A.I.; Persson, B.N.J. Resonant Photon Tunneling Enhancement of the van der Waals Friction. *Phys. Rev. Lett.* **2003**, *91*, 106101. [[CrossRef](#)]
17. Volokitin, A.I.; Persson, B.N.J. Adsorbate-Induced Enhancement of Electrostatic Noncontact Friction. *Phys. Rev. Lett.* **2005**, *94*, 086104. [[CrossRef](#)]
18. Volokitin, A.; Persson, B. Near-field radiative heat transfer and noncontact friction. *Rev. Mod. Phys.* **2007**, *79*, 1291–1329. [[CrossRef](#)]
19. Volokitin, A.I.; Persson, B.N.J. Theory of the interaction forces and the radiative heat transfer between moving bodies. *Phys. Rev. B* **2008**, *78*, 155437. [[CrossRef](#)]
20. Volokitin, A.; Persson, B.N.J. Quantum Friction. *Phys. Rev. Lett.* **2011**, *106*, 094502. [[CrossRef](#)]
21. Despoja, V.; Echenique, P.M.; Šunjić, M. Nonlocal microscopic theory of quantum friction between parallel metallic slabs. *Phys. Rev. B* **2011**, *83*, 205424. [[CrossRef](#)]
22. Fariás, M.B.; Kort-Kamp, W.J.M.; Dalvit, D.A.R. Quantum friction in two-dimensional topological materials. *Phys. Rev. B* **2018**, *97*, 161407. [[CrossRef](#)]
23. Novoselov, K.S.; Geim, A.K.; Morozov, S.V.; Jiang, D.; Zhang, Y.; Dubonos, S.V.; Grigorieva, I.V.; Firsov, A.A. Electric field effect in atomically thin carbon films. *Science* **2004**, *306*, 666–669. [[CrossRef](#)] [[PubMed](#)]

24. Dell'Anna, L.; Merano, M. Clausius-Mossotti Lorentz-Lorenz relations and retardation effects for two-dimensional crystals. *Phys. Rev. A* **2016**, *93*, 053808. [[CrossRef](#)]
25. Novoselov, K.S.; Geim, A.K.; Morozov, S.V.; Jiang, D.; Katsnelson, M.I.; Grigorieva, I.V.; Dubonos, S.V.; Firsov, A.A. Two-dimensional gas of massless Dirac fermions in graphene. *Nature* **2005**, *438*, 197–200. [[CrossRef](#)]
26. Zhang, Y.B.; Tan, Y.W.; Stormer, H.L.; Kim, P. Experimental observation of the quantum Hall effect and Berry's phase in graphene. *Nature* **2005**, *438*, 201. [[CrossRef](#)]
27. Geim, A.K.; Novoselov, K.S. The rise of graphene. In *Nanoscience and Technology*; World Scientific: Singapore, 2009; pp. 11–19.
28. Berger, C.; Song, Z.; Li, X.; Wu, X.; Brown, N.; Naud, C.; Mayou, D.; Li, T.; Hass, J.; Marchenkov, A.N.; et al. Electronic confinement and coherence in patterned epitaxial graphene. *Science* **2006**, *312*, 1191–1196. [[CrossRef](#)] [[PubMed](#)]
29. Freitag, M.; Low, T.; Xia, F.; Avouris, P. Photoconductivity of biased graphene. *Nat. Photon* **2013**, *7*, 53–59. [[CrossRef](#)]
30. Stauber, T.; Peres, N.M.R.; Geim, A.K. Optical conductivity of graphene in the visible region of the spectrum. *Phys. Rev. B* **2008**, *78*, 085432. [[CrossRef](#)]
31. Falkovsky, L.A. Optical properties of graphene. *J. Phys. Conf. Ser.* **2008**, *129*, 012004. [[CrossRef](#)]
32. Falkovsky, L.A.; Pershoguba, S. Optical far-infrared properties of a graphene monolayer and multilayer. *Phys. Rev. B* **2007**, *76*, 153410. [[CrossRef](#)]
33. Mikhailov, S.A.; Ziegler, K.G. New Electromagnetic Mode in Graphene. *Phys. Rev. Lett.* **2007**, *99*, 016803. [[CrossRef](#)] [[PubMed](#)]
34. Ju, L.; Geng, B.; Hornng, J.; Girit, C.; Martin, M.; Hao, Z.; Bechtel, H.A.; Liang, X.; Zettl, A.; Shen, Y.-R.; et al. Graphene plasmonics for tunable terahertz metamaterials. *Nat. Nanotechnol.* **2011**, *6*, 630. [[CrossRef](#)]
35. Jablan, M.; Buljan, H.; Soljačić, M. Plasmonics in graphene at infrared frequencies. *Phys. Rev. B* **2009**, *80*, 245435. [[CrossRef](#)]
36. Wang, T.-B.; Liu, N.-H.; Liu, J.-T.; Yu, T.-B. Quantum friction controlled by plasmons between graphene sheets. *Eur. Phys. J. B* **2014**, *87*, 185. [[CrossRef](#)]
37. Zhang, C.J.; Zhou, T.; Du, X.P.; Wang, T.B.; Liu, N.H. Enhancement of quantum friction via coupling of surface phonon polariton and graphene plasmons. *Acta Phys. Sin.* **2016**, *65*, 236801. [[CrossRef](#)]
38. Farias, M.B.; Fosco, C.D.; Lombardo, F.C.; Mazzitelli, F. Quantum friction between graphene sheets. *Phys. Rev. D* **2017**, *95*, 065012. [[CrossRef](#)]
39. Despoja, V.; Echenique, P.M.; Šunjić, M. Quantum friction between oscillating crystal slabs: Graphene monolayers on dielectric substrates. *Phys. Rev. B* **2018**, *98*, 125405. [[CrossRef](#)]
40. Luo, R.; Yang, J.-R.; Wang, T.-B.; Zhang, D.-J.; Liu, W.-X.; Yu, T.-B.; Liao, Q.-H. Enhancement of Casimir friction between graphene-covered hyperbolic materials. *Phys. Lett. A* **2021**, *387*, 127006. [[CrossRef](#)]
41. Fu, L.; Kane, C.L. Superconducting Proximity Effect and Majorana Fermions at the Surface of a Topological Insulator. *Phys. Rev. Lett.* **2008**, *100*, 096407. [[CrossRef](#)]
42. Qi, X.-L.; Zhang, S.-C. The quantum spin Hall effect and topological insulators. *Phys. Today* **2010**, *63*, 33–38. [[CrossRef](#)]
43. Hasan, M.Z.; Kane, C.L. Topological insulators. *Rev. Mod. Phys.* **2010**, *82*, 3045. [[CrossRef](#)]
44. Qi, X.L.; Zhang, S.C. Topological insulators and superconductors. *Rev. Mod. Phys.* **2011**, *83*, 1057. [[CrossRef](#)]
45. Karch, A. Surface plasmon and topological insulators. *Phys. Rev. B* **2011**, *83*, 245432. [[CrossRef](#)]
46. Fu, L.; Kane, C.L. Topological insulators with inversion symmetry. *Phys. Rev. B* **2007**, *76*, 045302. [[CrossRef](#)]
47. Hsieh, D.; Qian, D.; Wray, L.; Xia, Y.; Hor, Y.S.; Cava, R.J.; Hasan, M.Z. A topological Dirac insulator in a quantum spin Hall phase. *Nature* **2008**, *452*, 970–974. [[CrossRef](#)] [[PubMed](#)]
48. Zhang, H.; Liu, C.-X.; Qi, X.-L.; Dai, X.; Fang, Z.; Zhang, S.-C. Topological insulators in Bi₂Se₃, Bi₂Te₃ and Sb₂Te₃ with a single Dirac cone on the surface. *Nat. Phys.* **2009**, *5*, 438–442. [[CrossRef](#)]
49. Xia, Y.; Qian, D.; Hsieh, D.; Wray, L.A.; Pal, A.; Lin, H.; Bansil, A.; Grauer, D.; Hor, Y.S.; Cava, R.J.; et al. Observation of a large-gap topological-insulator class with a single Dirac cone on the surface. *Nat. Phys.* **2009**, *5*, 398–402. [[CrossRef](#)]
50. Hong, S.S.; Kundhikanjana, W.; Cha, J.J.; Lai, K.J.; Kong, D.S.; Meister, S.; Kelly, M.A.; Shen, Z.X.; Cui, Y. Ultrathin Topological Insulator Bi₂Se₃ Nanoribbons Exfoliated by Atomic Force Microscopy. *Nano Lett.* **2010**, *10*, 3118. [[CrossRef](#)]
51. Kong, D.; Dang, W.; Cha, J.J.; Li, H.; Meister, S.; Peng, H.; Liu, Z.; Cui, Y. Few-Layer Nanoplates of Bi₂Se₃ and Bi₂Te₃ with Highly Tunable Chemical Potential. *Nano Lett.* **2010**, *10*, 2245–2250. [[CrossRef](#)]
52. LaForge, A.D.; Frenzel, A.; Pursley, B.; Lin, T.; Liu, X.; Shi, J.; Basov, D.N. Optical characterization of Bi₂Se₃ in a magnetic field: Infrared evidence for magnetoelectric coupling in a topological insulator material. *Phys. Rev. B* **2010**, *81*, 125120. [[CrossRef](#)]
53. Akrap, A.; Tran, M.; Ubaldini, A.; Teyssier, J.; Giannini, E.; Van Der Marel, D.; Lerch, P.; Homes, C.C. Optical properties of Bi₂Te₂Se at ambient and high pressures. *Phys. Rev. B* **2012**, *86*, 235207. [[CrossRef](#)]
54. Wei, C.; Ren, S.F. Phonons of single quintuple Bi₂Te₃ and Bi₂Se₃ films and bulk materials. *Phys. Rev. B* **2011**, *83*, 094301. [[CrossRef](#)]
55. Zhou, L.; Carbotte, J.P. Hexagonal warping on spin texture, Hall conductivity and circular dichroism of topological Insulators. *Phys. Rev. B* **2014**, *89*, 165420. [[CrossRef](#)]
56. Wu, J.-S.; Basov, D.N.; Fogler, M. Topological insulators are tunable waveguides for hyperbolic polaritons. *Phys. Rev. B* **2015**, *92*, 205430. [[CrossRef](#)]
57. Ilic, O.; Jablan, M.; Joannopoulos, J.D.; Celanovic, I.; Buljan, H.; Soljačić, M. Near-field thermal radiation transfer controlled by plasmons in graphene. *Phys. Rev. B* **2012**, *85*, 155422. [[CrossRef](#)]
58. Zhao, B.; Guizal, B.; Zhang, Z.M.; Fan, S.; Antezza, M. Near-field heat transfer between graphene/hBN multilayers. *Phys. Rev. B* **2017**, *95*, 245437. [[CrossRef](#)]

59. Richter, W.; Becker, C.R. A Raman and far-infrared investigation of phonons in the rhombohedral V_2-VI_3 compounds Bi_2Te_3 , Bi_2Se_3 , Sb_2Te_3 and $Bi_2(Te_{1-x}Se_x)_3$ ($0 < x < 1$), $(Bi_{1-y}Sb_y)_2Te_3$ ($0 < y < 1$). *Phys. Status Solidi* **1977**, *84*, 619–628. [[CrossRef](#)]
60. Di Pietro, P.; Vitucci, F.M.; Nicoletti, D.; Baldassarre, L.; Calvani, P.; Cava, R.; Hor, Y.S.; Schade, U.; Lupi, S. Optical conductivity of bismuth-based topological insulators. *Phys. Rev. B* **2012**, *86*, 045439. [[CrossRef](#)]